

# Observation of the Dissipative Parametric Gain in a GaAs/AlGaAs Superlattice

Vladislovas Čižas,<sup>1</sup> Liudvikas Subačius,<sup>1</sup> Natalia V. Alexeeva,<sup>1</sup> Dalius Seliuta,<sup>1</sup>  
Timo Hyart,<sup>2,3</sup> Klaus Köhler,<sup>4</sup> Kirill N. Alekseev,<sup>1,5,\*</sup> and Gintaras Valušis<sup>1,6,†</sup>

<sup>1</sup>*Department of Optoelectronics, Center for Physical Sciences and Technology, Saulėtekio Ave. 3, LT-10257, Vilnius, Lithuania*

<sup>2</sup>*International Research Centre MagTop, Institute of Physics,*

*Polish Academy of Sciences, Al. Lotników 32/46, 02-668 Warsaw, Poland*

<sup>3</sup>*Department of Applied Physics, Aalto University, 00076 Aalto, Espoo, Finland*

<sup>4</sup>*Fraunhofer-Institut für Angewandte Festkörperphysik, Tullastrasse 72, Freiburg D-79108, Germany*

<sup>5</sup>*Department of Physics, Loughborough University, Loughborough LE11 3TU, United Kingdom*

<sup>6</sup>*Institute of Photonics and Nanotechnology, Department of Physics,  
Vilnius University, Saulėtekio Ave. 3, LT-10257 Vilnius, Lithuania*

Parametric generation of oscillations and waves is a paradigm, which is known to be realized in various physical systems. Unique properties of quantum superlattices allow to investigate high-frequency phenomena induced by the Bragg reflections and negative differential velocity of the miniband electrons. Effects of parametric gain in the superlattices at different strengths of dissipation have been earlier discussed in a number of theoretical works, but their experimental demonstrations are so far absent. Here, we report on the first observation of the dissipative parametric generation in a subcritically doped GaAs/AlGaAs superlattice subjected to a dc bias and a microwave pump. We argue that the dissipative parametric mechanism originates from a periodic variation of the negative differential velocity. It enforces excitation of slow electrostatic waves in the superlattice which provide a significant enhancement of the gain coefficient. This work paves the way for a development of a miniature solid-state parametric generator of GHz–THz frequencies operating at room temperature.

*Introduction.*—Parametric generation is a paradigm, known to be realized in various physical systems ranging from electronic circuits up to nonlinear optics. A large pump tone of the frequency  $\omega_0$  causes a periodic variation of a reactive element, which through mechanism of parametric resonance results in the degenerate  $2\omega_1 = \omega_0$  or nondegenerate  $\omega_1 + \omega_2 = \omega_0$  processes of regenerative amplification, and thus the both modes 1&2 can self-oscillate [1, 2]. Positive gain can also be reached in the phase-sensitive process of frequency up-conversion  $\omega_2 + \omega_0 = \omega_1$ , but such amplification is not regenerative and instead is governed by the familiar Manley-Rowe relations for powers associated with each of the modes [3].

However, there also exists less known dissipative parametric mechanism associated with a periodic variation of a nonlinear resistance, and it is often responsible for the generation of subharmonics in electric circuits modelled by driven nonlinear oscillators [4]. This mechanism requires that the system visits the state of negative differential resistance during part of the ac pump period [4, 5]. In the case of several modes, electric powers associated with every frequency are connected by the Pantell relations, which explicitly involve the differential conductance of nonlinear resistive circuit [6].

Quantum semiconductor superlattices (SLs) [7] can be found as a unique platform to meet the aforesaid condition. In these artificial crystals, miniband electrons can perform electrically driven high-frequency oscillations caused by the Bragg reflections [8]. The major focus is on the dc field induced Bloch oscillations, detectable both in time [9] and in space [10], and on the related dissipative phenomenon of Bloch gain [11]. The

electron drift velocity ( $v$ ) depends on the electric field following a nonlinear curve that above a certain critical field ( $E_{\text{cr}}$ ) demonstrates the negative differential velocity (NDV) [7, 12]. This active Esaki-Tsu nonlinearity is able to provide an efficient multiplication of the microwave input frequency in SL-based devices [13]. It was a significant progress to realize such THz frequency multipliers and mixers experimentally and obtain reasonable power output suitable for various applications [14–16].

Theories of parametric amplification and generation of high frequencies in quantum SLs exist for more than 40 years [17–26], and include, along with the earlier contributions [17–19], the thorough analysis of the degenerate [20, 21], nondegenerate [22] and multifrequency [23] parametric processes. Overall, the amplification is caused by the electronic Bragg reflections in the narrow energy band; it was predicted to be multiphoton and to exist for a very wide range of the pump frequencies ( $\omega_0$ ) that covers significant parts of GHz and THz frequency domains [20]. Nevertheless, microscopic physical mechanisms behind the parametric gain were found to be distinct whether  $\omega_0\tau > 1$  or  $\omega_0\tau \ll 1$  ( $\tau \simeq 200$  fs is a characteristic relaxation time at room temperature [11, 14]). In the case of high-frequency pump  $\omega_0\tau > 1$ , the parametric gain has its origin in a periodic variation of the effective electron mass and specific kinetic inductance of the miniband electrons [20, 24]. Furthermore, in the limit of small dissipation ( $\omega_0\tau \gg 1$ ), the Manley-Rowe relations are satisfied [22].

The behaviour is quite different in the limit of strong dissipation ( $\omega_0\tau \ll 1$ ), which corresponds to GHz pump frequencies [22, 25, 26]. Now not only down-conversion

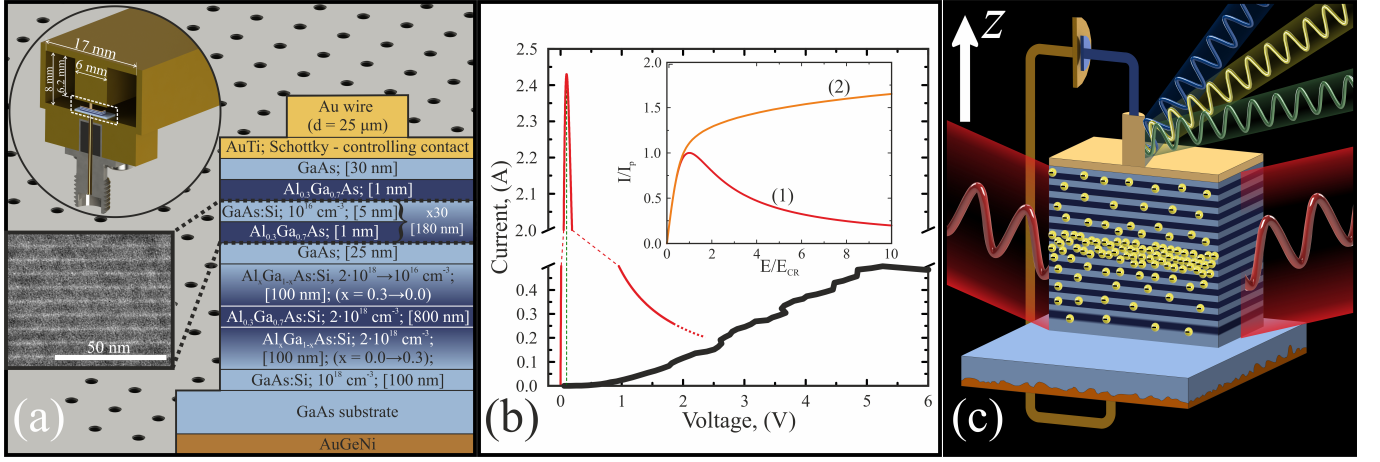


FIG. 1. **(a)**: Architecture of the GaAs/AlGaAs device where SL sandwiched between the AuTi Schottky contact from the top and the heterojunction from the bottom. To deliver the incident microwave to the structure, it was placed along the wide wall of a single-ridged waveguide of  $17 \times 8 \text{ mm}$ . Inset: TEM image of the superlattice. **(b)**: The measured  $I$ - $V$  characteristic of the SL device (thick black) in comparison with the ideal Esaki-Tsu  $I$ - $V$  characteristic (thin red). The vertical (dashed green) line marks the critical voltage ( $E_{cr}L \approx 0.1 \text{ V}$ ), for which the peak current  $I_p \approx 2.4 \text{ A}$  is reached. Inset: The Esaki-Tsu curve (1, red) versus the calculated  $I$ - $V$  characteristic of SL with ohmic injecting contact (2, orange). Notice that the experimental  $I$ - $V$  curve runs significantly below  $I_p$ , which is opposite to the behaviour of  $I$ - $V$  characteristics in the case of ohmic contacts. This points to nonohmic nature of contacts in our SL device. **(c)**: Sketch of the parametric generation in the SL device. Strong electromagnetic wave is coupled with electron plasma of the dc biased SL. The electric field component of this pump wave, directed along the SL axis  $z$ , parametrically interacts with the miniband electrons and excites a dozen of growing waves at frequencies satisfying the parametric conservation relations for photons [Eq. (1)]. The generated longitudinal electrostatic waves propagate along  $z$  at the electron drift velocity before being converted to radiation through the wire antenna. Spatial modulation of the electron density associated with only one of such slow waves is shown schematically.

but also up-conversion process can provide regenerative amplification [19, 22]. This dissipative parametric gain in SLs [22, 25, 26], while being in essence similar to that in nonlinear resistors, still relies on a periodic switching to the NDV state rather than on negative values of the differential conductance as in [6]. Indeed, an account of space charge effects in the basic transport model reveals that the static differential conductance of the moderately doped quantum SL is always positive [27], in agreement with the earlier findings [28, 29]. Despite decades of fruitful theoretical developments, there was no experimental evidence of the parametric gain effects in SLs so far.

In this Letter, we report on the first experimental observation of the dissipative parametric generation in a SL device subjected to a dc bias and a microwave pump. We detect both the degenerate and nondegenerate multiphoton parametric processes, together with signatures of large-signal gain effects. In this room temperature experiment, we use a special design of the device composed of a wide miniband GaAs/AlGaAs SL with asymmetric nonohmic contacts, allowing to make the electric field profile within the active part of the structure more uniform. We find that net optical gain for this parametric device can be almost thousand times greater than it follows from the earlier estimate [20], and argue that the enhancement originates from slow propagation of the in-

trinsic electrostatic waves inside the SL [30].

*Superlattice design and characterization.*—Experiments were performed using GaAs/AlGaAs SL structure given in Fig. 1(a). It contains 30 periods of 5 nm GaAs:Si quantum wells ( $10^{16} \text{ cm}^{-3}$ ) separated by 1 nm  $\text{Al}_{0.3}\text{Ga}_{0.7}\text{As}$  barriers to enable a wide miniband of 104 meV. The AuTi Schottky contact was fabricated on top of the structure, while from the SL bottom, GaAs/AlGaAs heterojunction was formed. The SL processed into a square mesa of  $80 \times 80 \mu\text{m}$  dimensions and of  $1.3 \mu\text{m}$  height using wet etching was then mounted inside the standard single-ridged waveguide. The gold wire of  $\simeq 25 \mu\text{m}$  was attached to the top contact of the SL to ensure proper coupling to microwaves and to serve for biasing of the structure. The bottom ohmic contact was connected to the coaxial line via filter. Measurements were performed employing a waveguide-based setup [31] relying on changes in the microwave transmission and reflection induced by the electron transport in the SL [32].

For this SL the product of the doping density  $N = 10^{16} \text{ cm}^{-3}$  and the length  $L = 180 \text{ nm}$  is below the specific critical value determining the onset of the travelling high-field domains,  $(NL)_{cr} = 7\epsilon E_{cr}/e = 2.7 \times 10^{11} \text{ cm}^{-2}$  [32, 35, 41]. Therefore, our subcritically doped SL operates in the electrically stable transport regime [42], in a similar way

to the well-known experiments [11, 43].

The experimental  $I-V$  characteristic of the SL device, measured employing electrical pulses of 20 ns duration, is presented in Fig. 1(b). It has positive slope, which is typical feature of electronic systems with NDV operating in the stable transport regime [27, 29, 44]. By taking this for granted, we find how a comparison of the experimental and so-called neutral  $I-V$  characteristics can be used to extract information on the nature of electric contacts of the SL. The neutral characteristic references to a special situation of the electric neutrality, when densities of the mobile and fixed ( $N$ ) charges coincide, electric field is homogeneous and contacts are absent [44]. In our case, this is the ideal Esaki-Tsu  $I-V$  characteristic, the shape of which directly follows the  $v(E)$  dependence. Next, both the calculations [27] and the experiments [11, 43] expose that  $I-V$  characteristics of SLs with ohmic contacts typically saturate either above the Esaki-Tsu peak current  $I_p$  [Fig. 1(b) inset] or on the level of  $I_p$  [inset of Fig. 1 in [11]]. On the contrary, the measured  $I-V$  characteristic runs significantly below  $I_p$  [Fig. 1(b)], indicating the nonohmic nature of contacts in our device. We attribute this nonohmicity to the presence of Schottky and shallow heterojunction barriers. Typically, the use of nonohmic contacts in NDV devices makes the electric field profile more uniform, and thus contributes to the better performance [44, 45]. In addition, the built-in voltage of 0.65 V increases the voltage drop across the SL by this amount.

*Experimental results and discussion.* – Experiment on the parametric generation in the SL device is sketched in Fig. 1(c). Strong electromagnetic wave passes through the SL along its layers, modulates the electron differential velocity, and by means of the dissipative parametric mechanism excites a spectrally rich coherent emission from the device into the output waveguide. In the earlier theoretical suggestions, the generated spectral components were assumed to be transverse electromagnetic modes of the external cavity (cf. Fig. 1 in [20]). Contrastingly, our device operates without such resonator and mainly relies on intrinsic longitudinal modes inside the SL that are growing from fluctuations of the electron plasma. We will return to the discussion of the origin and significance of these intrinsic modes after consideration of the generated frequencies in the light of the major predictions of the theory.

The measured emission spectrum for the case of 8.45 GHz pump is presented in Fig. 2 (vertical panel). The strength of ac field inside the SL was estimated to be  $\simeq 8E_{cr}$  [32]. Along with the pump and its harmonics up to the 4<sup>th</sup> order, the spectrum also contains additional 11 emission lines. The prerequisite for an enforcement of the stimulated emission at these discrete frequencies is a positive gain for infinitesimal signals. The theory states that the small-signal parametric gain in SLs can arise only for the frequencies  $\omega_{1,2}$  that are connected to the

pump frequency as

$$\omega_1 \pm \omega_2 = n_{\pm}\omega_0, \quad 2\omega_1 = n_0\omega_0, \quad (1)$$

where  $n_+$ ,  $n_-$  are positive integers and  $n_0$  is odd [20, 22, 26]. The existence of the parametric relations with  $n \neq 1$  is a definitely notable property of the quantum superlattice nonlinearity. Whereas generation of the half-harmonics and spontaneous down-conversions with various  $n_+$  are universal signatures of the parametric gain in SLs [20], the appearance of self-oscillations at both frequencies involved in the up-conversion processes [Eq. (1) with  $n_- \geq 1$ ] is a remarkable property of the dissipative mechanism [19, 22].

The data and links displayed in Fig. 2 affirm that the observed parametric emission lines (black and orange) satisfy the photon energy conservation relations of Eqs. (1), and thus can include many photons of the pump ( $n > 1$ ). Surprisingly, we also found that almost every spectral line participates in several multiphoton processes simultaneously. For instance, the frequency 28.20 GHz is

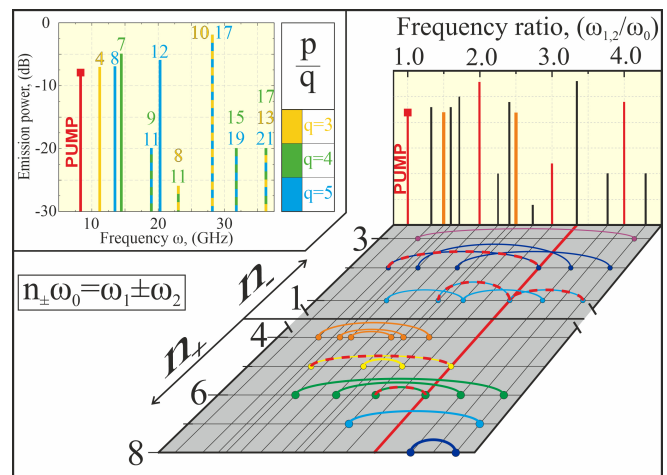


FIG. 2. The spectrum of the frequencies generated in SL under the action 8.45 GHz pump and bias of 0.3 V. The frequencies are scaled to the pump frequency (vertical panel). The spectral lines corresponding to the pump and its multiplication (red), the sub-harmonics (orange), and to the non-degenerate parametric processes (black) are displayed. The 1/2-harmonic is not visible due to cut-off characteristics of the output waveguide. The links in the horizontal panel indicate that the observed emission lines follow the spectrum of the small-signal parametric gain [Eq. (1)]. Multiphoton and multiple wave mixing phenomena (red dashed lines), related to the generation at 28.20 GHz (horizontal solid red line), are further exemplified in Eqs. (2). Inset: The frequencies classified according to the pump fractions [Eq. (3)]. The corresponding numerators  $p$  are shown nearby their spectral chart, while the denominators  $q$  are defined following the color chart.

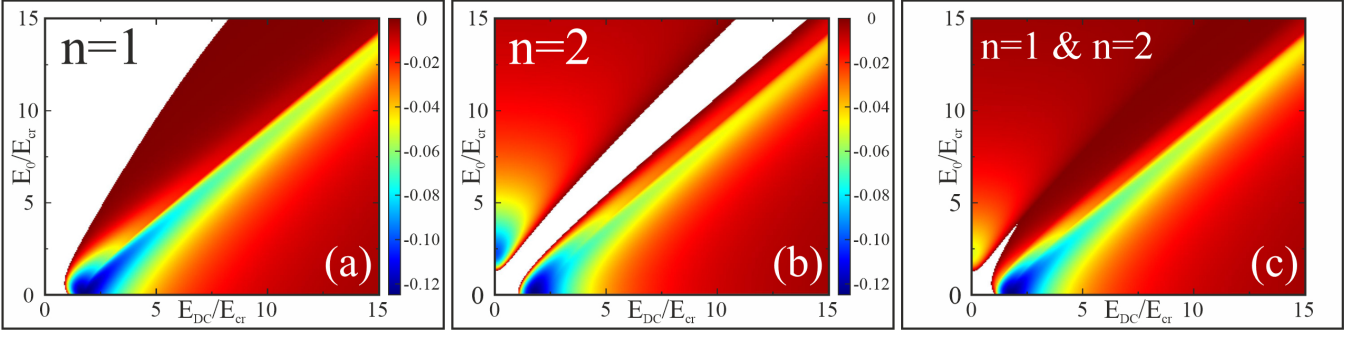


FIG. 3. **(a-b)**: The areas and magnitudes of gain  $\mu_n < 0$  (color) in the plane of dc bias  $E_{dc}$  and pump field amplitude  $E_0$  for  $n = 1$  (a) and  $n = 2$  (b). The calculated high-frequency mobilities  $\mu_n$  are presented in units of the superlattice Drude mobility ( $2v_p/E_{cr}$ ), and the dc and ac electric fields are scaled to the critical field  $E_{cr}$ . Blank areas everywhere correspond to absorption ( $\mu_n > 0$ ). **(c)**: Overlapping of the areas corresponding to both  $\mu_1 < 0$  and  $\mu_2 < 0$  (color) in the same plane. The figure illustrates an overall extension of the gain area with the only boundary at low fields, in the case when two parametric processes are simultaneously realised in the SL.

generated in the following processes (cf. Fig. 2):

$$\left\{ \begin{array}{l} 28.20 + 23.05 = 6 \times 8.45 \text{ GHz (8-photons),} \\ 28.20 + 13.45 = 5 \times 8.45 \text{ GHz (7-photons),} \\ 28.20 - 11.20 = 2 \times 8.45 \text{ GHz (4-photons),} \\ 28.20 - 20.30 = 1 \times 8.45 \text{ GHz (3-photons),} \\ 36.25 - 28.20 = 1 \times 8.45 \text{ GHz (3-photons).} \end{array} \right. \quad (2)$$

This unusual behaviour in SLs is in sharp contrast to the parametric generation in conventional optical systems, where multiphoton effects involving the pump ( $n\hbar\omega_0$ ) are virtually absent, and even multi-step frequency cascades [46] are well described by the Manley-Rowe relations [47, 48]. As a consequence, optical parametric generation of the frequencies involved in the up-conversion processes with several pump photons ( $n_- = 2, 3$ ) is unlikely realizable [48], but such emission lines are readily observable in the SL, see Fig. 2.

Furthermore, the measured emission spectrum can bear signatures of generation effects that go beyond the linear response in signal strengths. In the case of large signals ( $\simeq E_{cr}$ ), it is predicted that new channels in parametric generation induce the fractional frequencies

$$\omega_1 = (p/q)\omega_0, \quad q > 2, \quad (3)$$

where  $p, q$  are integers [21, 23]. In particular, the subharmonics  $p\omega_0/3$  and  $p\omega_0/4$  can arise due to effects that are quadratic and cubic in the signal strength, respectively [21]. Analysis of the data (Fig. 2 inset) unveils this type of frequencies and thus experimentally confirms involvement in the large signal regime. Similar emission spectra, the spectral components of which do fit Eqs. (1) and (3), were observed for other pump frequencies close to 10 GHz. Different multiphoton parametric processes in SL can be also distinguished by comparing their input-output power dependencies [32]. At

the present state of the art, however, this method is less informative than the used spectroscopic approach.

*Theoretical justification.*—To get deeper insight into the role of the observed multiple simultaneous parametric processes, we calculate and compare the high-frequency electron mobilities  $\mu_n(E_{dc}, E_0)$  for two processes with  $n = 1$  and  $n = 2$  separately [Eq. (1)], and also for their combination [cf. Eqs. (2)]. The total pump electric field was assumed to be the sum of dc bias  $E_{dc}$  and strong ac field  $E_0 \cos(\omega_0 t)$ , where  $\omega_0 \tau \ll 1$  [32]. The calculated areas of gain ( $\mu_n < 0$ ) and absorption ( $\mu_n > 0$ ) in the plain  $E_0$ - $E_{dc}$  are presented in Fig. 3. For the both single parametric processes shown in the subplots (a) and (b), there exist wide blank areas of no-gain, which effectively can cause appearance and disappearance of the amplification at relatively large values of either  $E_0$  or  $E_{dc}$ . However, in the case the two parametric processes run simultaneously, the gain area expands and the blank area survives only for rather weak applied fields  $\lesssim E_{cr}$  [Fig. 3(c)]. This determines a well-defined threshold line for the positive gain when  $E_0 \simeq E_{dc} \simeq E_{cr}$ . Therefore, an account of the multiple processes in SLs restores intuitive correspondence with the condition of dissipative parametric amplification in nonlinear resistors.

We turn to the origin of the intrinsic electrostatic modes [Fig. 1(c)] and their contribution to the net optical gain. Generally, every such electrostatic mode propagates at the drift velocity of electrons [49], and represents an undamped excitation of the solid state plasma in condition of NDV [50]. Specifically for the Esaki-Tsu active nonlinearity, it is known as the drift-relaxation self-mode of SL [30] caused by the Bragg reflections of the mini-band electrons [51]. We apply this concept to the case of the dissipative parametric gain.

Consider an intrinsic longitudinal mode which frequency satisfies one of the parametric relations of Eqs. (1)



at some fixed photon number  $n$ . If the corresponding  $\mu_n < 0$ , in the linear stage small fluctuations of the electric field grow exponentially while electron flow propagates with the drift velocity  $v$  through the sample of the length  $L$ . The growth rate of the electrostatic wave is determined by the product of the dielectric relaxation frequency  $(eN\mu_n)/\epsilon$  and the electron transit time  $L/v$  [52]. Therefore, the gain coefficient  $\beta_n$ , defined by means of the Beer law  $I_{\text{out}} = I_{\text{in}} \exp(-\beta z)$ , can be estimated as

$$\beta_n = \frac{2eN\mu_n}{\epsilon v}. \quad (4)$$

Remarkable, the direct substitution  $v/2 \simeq v_p \rightarrow c'$  transforms the right-hand side of Eq. (4) into the corresponding gain coefficient of the electromagnetic mode traveling at speed of light in the semiconductor  $c' = c/n_r$  ( $n_r$  is the average refractive index of SL) [20, 53]. Since  $v_p/c' \simeq 10^{-3}$  contribution of the slow electrostatic modes to the net optical gain can prevail. By assuming  $\mu_1/\mu_0 \approx -0.02$  for the 3-photon parametric processes [Fig. 3(a)] we obtain from Eq. (4) large gain  $\beta_1 \gtrsim 10^4 \text{ cm}^{-1}$  for the corresponding slow modes.

Finally, the generated electrostatic modes are transformed to the coherent electromagnetic radiation through a wire antenna bonded to the SL [Fig. 1(c)]. It is worth noticing that similar phase-preserving conversions of electromagnetic waves to plasmons and back have been demonstrated in nanometric field effect transistors [54, 55].

*Conclusion.*—We observed and explained unusual parametric generation in a quantum optoelectronic system with strong dissipation when the Manley-Rowe relations are broken. We showed that intensive microwave pumping of the GaAs/AlGaAs superlattice stimulates dissipative parametric gain at room temperature, manifesting itself as a steady coherent emission at various fractional harmonics of the pump frequency. Unusually, this device starts to self-oscillate in up-conversion processes as easy as in down-conversion ones. We also revealed the significance of the undamped drift-relaxation modes for the amplification mechanism in the superlattice. These slow plasma waves can provide large gain of  $\simeq 10^4 \text{ cm}^{-1}$  and more, thus enabling multiphoton generation in the cavityless configuration. Our experiments confirmed core predictions of the existing theory of dissipative parametric amplification at GHz frequencies, and also further stretched its limits by describing the multiple parametric processes. At once, semiconductor quantum SLs hold the promise of room temperature parametric amplification in the technologically important sub-THz range and beyond [20].

We are sincerely grateful to Martynas Skapas, Sandra Stanionytė and Remigijus Juškėnas for superlattice characterization; Linas Minkevičius, Vladimir Maksimenko, and Miron S. Kagan for illuminating discussions. Research activities of K.N.A. were partially funded by Mar-

ius Jakulis Jason Foundation and T.H. was supported, in part, by Foundation for Polish Science through the IRA Programme co-financed by EU within SG OP.

---

\* kirill.alekseev@ftmc.lt (theory)

† gintaras.valusis@ftmc.lt (experiment)

- [1] J. W. Strutt, Proc. R. Soc. London **41**, 275 (1887).
- [2] M. I. Rabinovich and D. I. Trubetskov, *Oscillations and Waves in Linear and Nonlinear Systems* (Springer Netherlands, 1989).
- [3] J. M. Manley and H. E. Rowe, Proc. IRE **44**, 904 (1956).
- [4] L. Mandelstam and N. Papalexi, Z. Phys. **73**, 223 (1932).
- [5] V. V. Migulin, V. I. Medvedev, E. R. Mustel, and V. N. Parygin, *Basic Theory of Oscillations* (Mir Publishers, Moscow, 1989).
- [6] R. H. Pantell, Proc. IRE **46**, 1910 (1958).
- [7] L. Esaki and R. Tsu, IBM J. Res. Dev. **14**, 61 (1970).
- [8] F. Bass and A. Tetervov, Physics Reports **140**, 237 (1986).
- [9] J. Feldmann, K. Leo, J. Shah, D. A. B. Miller, J. E. Cunningham, T. Meier, G. von Plessen, A. Schulze, P. Thomas, and S. Schmitt-Rink, Phys. Rev. B **46**, 7252 (1992).
- [10] V. G. Lyssenko, G. Valušis, F. Löser, T. Hasche, K. Leo, M. M. Dignam, and K. Köhler, Phys. Rev. Lett. **79**, 301 (1997).
- [11] P. G. Savvidis, B. Kolasa, G. Lee, and S. J. Allen, Phys. Rev. Lett. **92**, 196802 (2004).
- [12] A. Sibille, J. F. Palmier, H. Wang, and F. Molloy, Phys. Rev. Lett. **64**, 52 (1990).
- [13] A. A. Ignatov and Y. A. Romanov, Phys. Status Solidi B **73**, 327 (1976).
- [14] K. F. Renk, B. I. Stahl, A. Rogl, T. Janzen, D. G. Pavel'ev, Y. I. Koshurinov, V. Ustinov, and A. Zhukov, Phys. Rev. Lett. **95**, 126801 (2005).
- [15] D. G. Paveliev, Y. I. Koshurinov, A. S. Ivanov, A. N. Panin, V. L. Vax, V. I. Gavrilenko, A. V. Antonov, V. M. Ustinov, and A. E. Zhukov, Semiconductors **46**, 121 (2012).
- [16] D. J. Hayton, A. Khudchenko, D. G. Pavelyev, J. N. Hovenier, A. Baryshev, J. R. Gao, T. Kao, Q. Hu, J. L. Reno, and V. Vaks, Appl. Phys. Lett. **103**, 051115 (2013).
- [17] V. V. Pavlovich, Sov. Phys. Solid State **19**, 54 (1977).
- [18] L. K. Orlov and Y. A. Romanov, Radiophysics and Quantum Electronics **23**, 942 (1980).
- [19] L. K. Orlov and Y. A. Romanov, Radiophysics and Quantum Electronics **25**, 506 (1982).
- [20] T. Hyart, A. V. Shorokhov, and K. N. Alekseev, Phys. Rev. Lett. **98**, 220404 (2007).
- [21] A. V. Shorokhov and K. N. Alekseev, Int. J. Mod. Phys. B **23**, 4448 (2009).
- [22] T. Hyart and K. N. Alekseev, Int. J. Mod. Phys. B **23**, 4403 (2009).
- [23] Y. A. Romanov and Y. Y. Romanova, Journal of Experimental and Theoretical Physics **91**, 1033 (2000).
- [24] T. Hyart, N. V. Alexeeva, A. Leppänen, and K. N. Alekseev, Appl. Phys. Lett. **89**, 132105 (2006).
- [25] K. N. Alekseev, M. V. Gorkunov, N. V. Demarina, T. Hyart, N. V. Alexeeva, and A. V. Shorokhov, EPL **73**, 934 (2006).

- [26] Y. A. Romanov, J. Y. Romanova, and L. G. Mouroukh, J. Appl. Phys. **99**, 013707 (2006).
- [27] V. A. Maksimenko, V. V. Makarov, A. A. Koronovskii, A. E. Hramov, R. Venckevičius, G. Valušis, A. G. Balanov, F. V. Kusmartsev, and K. N. Alekseev, JETP Lett. **103**, 465 (2016).
- [28] W. Shockley, Bell Syst. Tech. J. **33**, 799 (1954).
- [29] H. Kroemer, Proc. IEEE **58**, 1844 (1970).
- [30] A. A. Ignatov and V. I. Shashkin, Sov. Phys. JETP **66**, 526 (1987).
- [31] L. Subačius, K. Jarašiūnas, P. Ščajev, and M. Kato, Measurement Science and Technology **26**, 125014 (2015).
- [32] See Supplemental Material at [URL will be inserted by publisher] for detailed description of the experimental setup, calculations of the HF mobilities, explanation of the NL-criterion, estimation of the ac-field strength inside the structure, and input-output power dependencies. It also provides the data related to Fig. 2 in the form of tables and includes Refs. [11, 25, 31, 33–40].
- [33] Y. Y. Romanova, Semiconductors **96**, 1451 (2012).
- [34] A. V. Shorokhov and K. N. Alekseev, Physica E: Low-dimensional Systems and Nanostructures **33**, 284 (2006).
- [35] A. A. Ignatov, V. I. Piskarev, and V. I. Shashkin, Sov. Phys. Semicond. **19**, 1345 (1985).
- [36] B. Rieder, *Semiclassical transport in semiconductor superlattices with boundaries*, Ph.D. thesis, University of Regensburg (2004).
- [37] C. Wang, M. J. Burek, Z. Lin, H. A. Atikian, V. Venkataraman, I. Huang, P. Stark, and M. Lončar, Optics Express **22**, 30924-30933 (2014).
- [38] H. Zhao, Q. An, X. Ye, B. H. Yu, Q. H. Zhang, F. Sun, Q. Y. Zhang, F. Yang, J. Guo, and J. Zhao., Nano Energy **82**, 105752 (2021).
- [39] Y. Du, S. N. Zhu, Y. Y. Zhu, P. Xu, C. Zhang, Y. B. Chen, Z. W. Liu, N. B. Minget, X. R. Zhang, F. F. Zhang, and S. Y. Zhang, Appl. Phys. Lett. **81**, 1573-1575 (2002).
- [40] R. Byer, Journal of Nonlinear Optical Physics and Materials **6**, 549-592 (1997).
- [41] H. Kroemer, Proc. IEEE **52**, 1736 (1964).
- [42] H. Kroemer, Proc. IEEE **53**, 1246 (1965).
- [43] A. Sibille, J. F. Palmier, F. Mollot, H. Wang, and J. C. Esnault, Phys. Rev. B **39**, 6272 (1989).
- [44] D. Dascălu, *Transient-time effects in unipolar solid-state devices* (Abacus Press, Kent, UK, 1974).
- [45] S. P. Yu, W. Tantraporn, and J. Young, IEEE Transactions on Electron Devices **18**, 88 (1971).
- [46] R. A. Andrews, H. Rabin and C. L. Tang, Phys. Rev. Lett. **25**, 902 (1970).
- [47] A. S. Chirkin, V. V. Volkov, G. D. Laptev, and E. Y. Morozov, Quantum Electronics **30**, 847 (2000).
- [48] S. M. Saltiel, A. A. Sukhorukov, and Y. S. Kivshar, *Multistep parametric processes in nonlinear optics*, Progress in Optics, Vol. 47, pp. 1–73, edited by E. Wolf (Elsevier, 2005).
- [49] M. A. Lampert, Journal of Applied Physics **27**, 5 (1956).
- [50] E. Schöll, *Nonequilibrium Phase Transitions in Semiconductors* (Springer, New York, 2012).
- [51] M. Büttiker and H. Thomas, Phys. Rev. Lett. **38**, 78 (1977).
- [52] W. Heinle, Solid-State Electron. **11**, 583 (1968).
- [53] A. Wacker, Phys. Rev. B **66**, 085326 (2002).
- [54] C. Drexler, N. Dyakonova, P. Olbrich, J. Karch, M. Schafberger, K. Karpierz, Y. Mityagin, M. B. Lifshits, F. Teppe, O. Klimenko, *et al.*, J. Appl. Phys. **111**, 124504 (2012).
- [55] Y. Matyushkin, S. Danilov, M. Moskotin, V. Belosevich, N. Kaurova, M. Rybin, E. D. Obraztsova, G. Fedorov, I. Gorbenko, V. Kachorovskii, *et al.*, Nano Letters **20**, 7296 (2020).

# Supplemental Material

## Observation of the Dissipative Parametric Gain in a GaAs/AlGaAs Superlattice

Vladislovas Čizas,<sup>1</sup> Liudvikas Subačius,<sup>1</sup> Natalia V. Alexeeva,<sup>1</sup> Dalius Seliuta,<sup>1</sup>  
Timo Hyart,<sup>2,3</sup> Klaus Köhler,<sup>4</sup> Kirill N. Alekseev,<sup>1,5</sup> and Gintaras Valušis<sup>1,6</sup>

<sup>1</sup>*Department of Optoelectronics, Center for Physical Sciences and Technology, Saulėtekio Ave. 3, LT-10257, Vilnius, Lithuania*

<sup>2</sup>*International Research Centre MagTop, Institute of Physics,*

*Polish Academy of Sciences, Al. Lotników 32/46, 02-668 Warsaw, Poland*

<sup>3</sup>*Department of Applied Physics, Aalto University, 00076 Aalto, Espoo, Finland*

<sup>4</sup>*Fraunhofer-Institut für Angewandte Festkörperphysik, Tullastraße 72, Freiburg D-79108, Germany*

<sup>5</sup>*Department of Physics, Loughborough University, Loughborough LE11 3TU, United Kingdom*

<sup>6</sup>*Institute of Photonics and Nanotechnology, Department of Physics,  
Vilnius University, Saulėtekio Ave. 3, LT-10257 Vilnius, Lithuania*

### CONTENTS

I. Superlattice design and experimental setup	1
II. NL-criterion for the case of ac-driven superlattice	2
III. Degenerate and nondegenerate amplification of microwaves in superlattices: Calculation of the high frequency mobility within the quasistatic approximation	3
A. Introduction to the problem	3
B. Summary of the main results on HF mobilities	4
C. Calculations of HF mobilities for the degenerate case	5
D. Calculations of HF mobilities for the nondegenerate cases	6
IV. Estimation of the pump electric field strength in the SL	7
V. The measured input-output power dependencies	8
VI. Figure 2 data in the form of two tables	8
References	10

### I. SUPERLATTICE DESIGN AND EXPERIMENTAL SETUP

Specially designed GaAs/AlGaAs superlattice (SL) was grown using molecular beam epitaxy technique on  $n$ -doped GaAs substrate ( $\sim 500 \mu\text{m}$ ;  $10^{18} \text{ cm}^{-3}$ ). The architecture of the SL structure is given in the right panel of Fig. 1. It contains 30 periods of moderately doped quantum wells GaAs:Si ( $5 \text{ nm}$ ;  $10^{16} \text{ cm}^{-3}$ ) separated by  $\text{Al}_{0.3}\text{Ga}_{0.7}\text{As}$  ( $1 \text{ nm}$ ) barriers and enabling thus a wide miniband ( $104 \text{ meV}$ ) in the SL. AuTi Schottky contact, following GaAs buffer layer ( $30 \text{ nm}$ ), were fabricated on the top of the structure. From the bottom side of the SL, GaAs ( $25 \text{ nm}$ ) layer with  $\text{Al}_x\text{Ga}_{1-x}\text{As}$  heterojunction was formed ( $100 \text{ nm}$ ; gradient-type alloy and concentration; for more details see inset in Fig. 1). The bottom contact on the substrate was Ohmic, realized by annealing of AuGeNi alloy.

The accuracy of the grown superlattice was checked by TEM and the images are presented in Fig. I. The SL processing was done using wet etching to fabricate square mesa of  $80 \times 80 \mu\text{m}$  dimensions and of  $1.3 \mu\text{m}$  height. The processed structure was mounted inside the standard single-ridged waveguide; the top contact of the superlattice was attached using  $\sim 25 \mu\text{m}$  Au wire to ensure suitable coupling with microwave electric fields simultaneously serving for biasing of the structure. The bottom contact was isolated via filter to diminish microwave radiation effect on the coaxial dc-biasing line.

Measurements were performed using microwave waveguide-based setup [1] relying on the change in transmitted and reflected microwaves induced by the carrier transport processes in the biased SL. The measurement setup is presented in Fig. 3. Microwave radiation of  $10 \text{ mW}$  power was delivered from a klystron generator operating within  $8.2 - 12.4 \text{ GHz}$  frequencies and transferred into the experimental setup via ferrite circulator. To achieve wide frequency range measurements, three different-size waveguide adapters [WR-90 (X-band) to WR-62 ( $K_u$ -band), WR-42 (K-band), and WR-28 ( $K_a$ -band)] were connected via waveguide switch. An impedance transformer was used to adjust the phase of the microwave radiation in the SL at selected frequency. It was realized by varying the distance

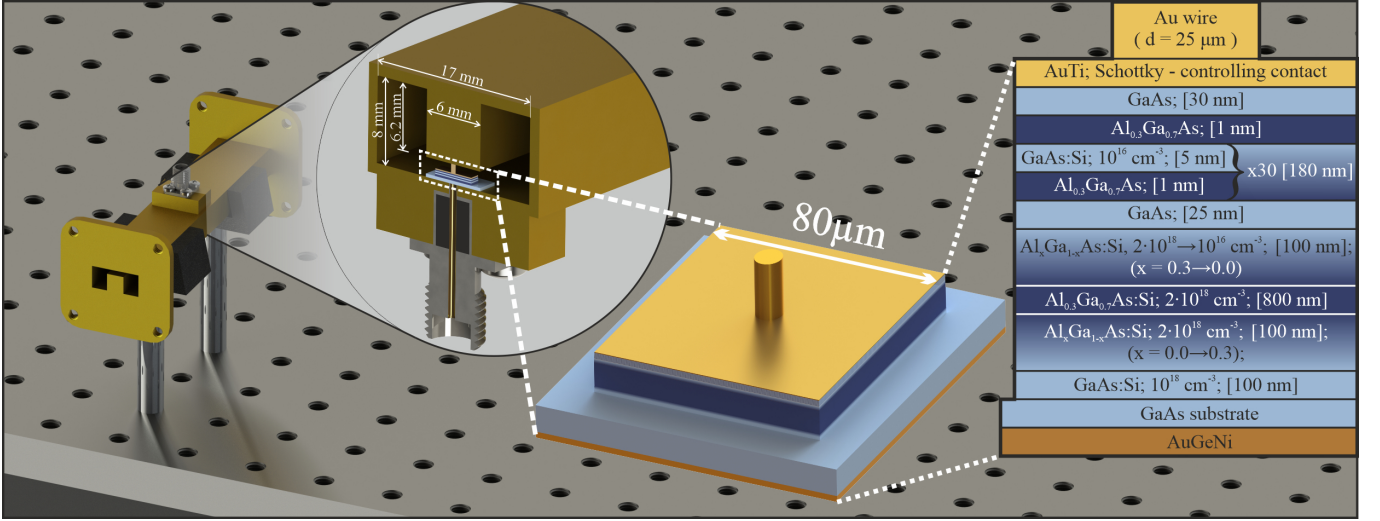


FIG. 1. Part of the measurement setup with enlarged view of the sample holder for mounting the structure. The sample was placed along the wide wall of a single-ridged waveguide with dimensions of  $17 \times 8$  mm to guide the incident microwave radiation. To provide the effective coupling of the radiation into the structure,  $25 \mu\text{m}$  diameter golden wire was bonded to the top contact serving also for application of the bias voltage over the SL. Bottom Ohmic contact of the SL was connected to coaxial line via filter. Total thickness of the grown structure was  $\sim 1.3 \mu\text{m}$ ; rectangular mesa of  $80 \times 80 \mu\text{m}$  was processed.

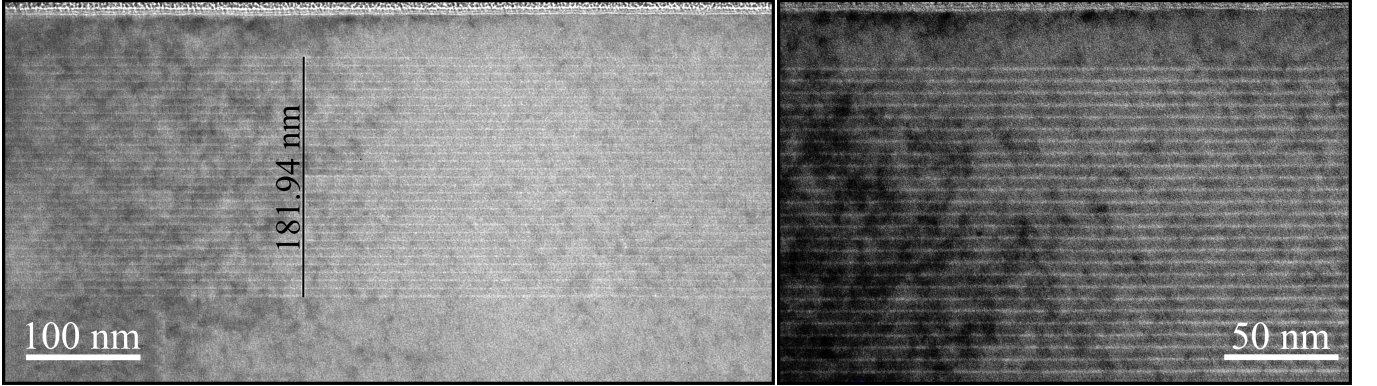


FIG. 2. TEM images of the superlattice taken at two different scales to justify accuracy of the fabricated structure. Length of 181.94 nm results in 6.06 nm superlattice period. The images are recorded in the microscope Tecnai G2 F20 X-TWIN (FEI Company, Netherlands). Sample for TEM imaging is prepared using FESEM-FIB Helios NanoLab 650 (FEI Company, Netherlands).

between two quartz quarter wave plates inside the transformer enabling hence to achieve maximal response signal from the SL under test.

The reflected signal analysis was monitored using calibrated Schottky diode detector. The frequency response was explored using C4-27 spectrum analyser. All experiments were performed at room temperature.

## II. NL-CRITERION FOR THE CASE OF AC-DRIVEN SUPERLATTICE

In the case of the Esaki-Tsu dependence of the drift velocity on the electric field and for

$$NL \leq \frac{7\epsilon E_{\text{cr}}}{e}, \quad (1)$$

no high-electric field domains are formed in the SL in conditions of NDV (here  $N$  is the electron concentration,  $L$  is the length of the SL,  $\epsilon = \epsilon_0\epsilon_r$  and  $\epsilon_r$  is the relative dielectric constant) [2, 3]. The criterium (1) has been formally



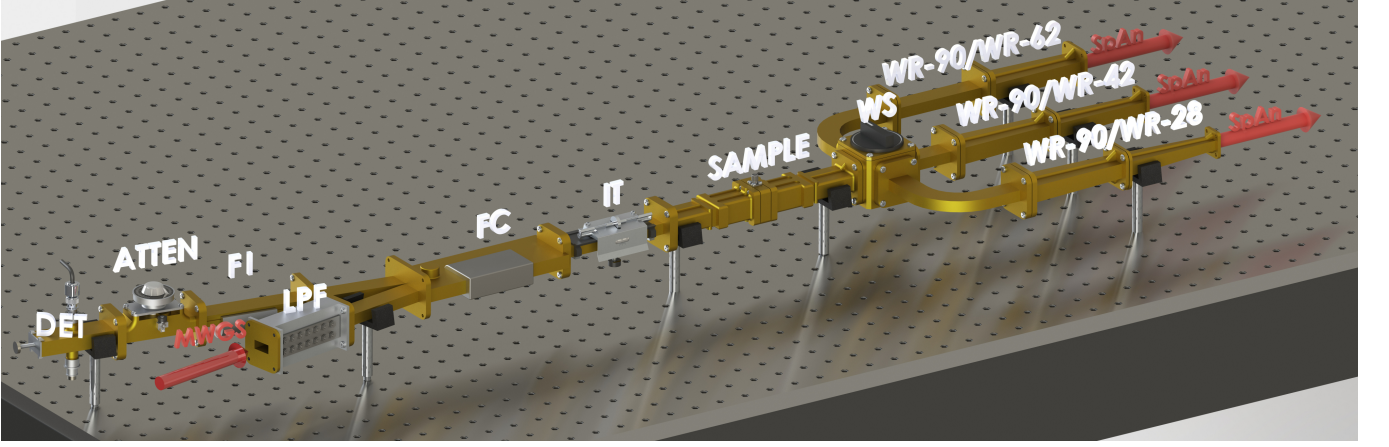


FIG. 3. Experimental setup. Microwave radiation generated by klystron (operating within 8.2 - 12.4 GHz frequency range), at (MWGS) input is transferred into experimental setup via ferrite circulator (FC). Low pass filter (LPF) is additionally used to remove parasitic high-frequency components. A waveguide switch (WS) was used to connect three WR-90/WR-XX waveguide adapters (WR-XX: WR-62, WR-42, WR-28) to spectrum analyser which allows to perform spectral measurements in a wide frequency range. Impedance transformer (IT) adjusted to excitation frequency was used to suppress reflections of the excitation signal and ensure maximal signal via proper adjustment of optimal phase at the sample. Reflected wave transient change monitoring was performed at Schottky-diode detector (DET), connected via attenuator (ATTN), ferrite circulator (FC) and isolator (FI). Sample holder of above-mentioned dimensions was connected via two adapters.

derived when only dc bias is applied, but it still can be easily extended to the case of the quasistatic ac electric field [Eq. (2)] for which  $\omega_0\tau \ll 1$ . Indeed, the miniband electrons interact with the quasistatic electric field essentially in the same manner as with the dc electric field, except the total dc+ac electric field is slowly sweeping within the range from  $E_{DC} - E_0$  to  $E_{DC} + E_0$  in the course of time. However, the inequality (1) actually states that the electric stability exists for any applied field strength (see, e.g., Sec. 1.4.1 in [4]). Therefore, this form of  $NL$ -criterion also works if quasistatic electric fields are applied to a quantum superlattice with proper parameters.

### III. DEGENERATE AND NONDEGENERATE AMPLIFICATION OF MICROWAVES IN SUPERLATTICES: CALCULATION OF THE HIGH FREQUENCY MOBILITY WITHIN THE QUASISTATIC APPROXIMATION

Our main aim here is to estimate the high-frequency (HF), small-signal parametric gain in units of the miniband Drude mobility. The major findings are summed up in Fig. 4.

#### A. Introduction to the problem

We assume that the total electric field  $E(t)$ , which is acting on miniband electrons, consists of the dc and ac pump

$$E_p(t) = E_{DC} + E_0 \cos(\omega_0 t) \quad (2)$$

and the ac probe  $E_{pr}(t)$  fields. We consider two situations for which either

$$E_{pr}(t) = E_1 \cos(\omega_1 t + \phi_1) + E_2 \cos(\omega_2 t + \phi_2) \quad \text{with} \quad \omega_1 \pm \omega_2 = n_{\pm} \omega_0 \quad (3)$$

or

$$E_{pr}(t) = E_1 \cos(\omega_1 t + \phi) \quad \text{with} \quad 2\omega_1 = n_0 \omega_0, \quad (4)$$

where  $n_{\pm}$  are positive integers and  $n_0$  is odd; the frequencies  $\omega_{1,2}$  in Eq. (3) are incommensurable. The cases of Eqs. (3) and (4) correspond to the nondegenerate and degenerate parametric amplifications, respectively. In the both cases all fields must be coherent and therefore the phase differences  $(\phi, \phi_{1,2})$  are well-defined constants. In what follows we suppose that the pump  $E_p(t)$  is arbitrary strong, while the probe field is weak ( $|E_{pr}| \ll |E_p|$ ). In contrast to a spontaneous process of frequency multiplication due to nonlinearity  $\omega_0 \rightarrow n\omega_0$ , the parametric amplification is

a stimulated processes for which influence of even very weak probe field cannot be ignored. In a single miniband superlattice, the electron drift velocity  $v$  depends on the dc electric field as

$$v(E_{\text{dc}}) = \frac{2v_p(E_{\text{dc}}/E_{\text{cr}})}{[1 + (E_{\text{dc}}/E_{\text{cr}})^2]}, \quad (5)$$

where  $v_p = \Delta d/4\hbar$  is the peak electron velocity (here  $d$  is the SL period,  $\Delta$  is the miniband width) and  $E_{\text{cr}} = \hbar/ed\tau$  is the Esaki-Tsu critical field ( $\tau$  is a characteristic relaxation time). In the quasistatic approximation that is valid for  $\omega_0\tau \ll 1$  and  $\omega_{1,2}\tau \ll 1$ , the drift velocity follows variations of the ac electric fields, and therefore the dependence of  $v$  on the total time-dependent field  $E(t)$  is given by Eq. (5) with account of the substitution  $E_{\text{dc}} \rightarrow E(t)$ .

Positive gain is defined in terms of the complex HF mobility  $\mu = \mu_r + i\mu_i$  as a response of the electron velocity  $v(t)$  to the probe ac field:

$$v = \Re[\mu E_1 e^{-i\omega_1 t}] = [\mu_r \cos(\omega_1 t) + \mu_i \sin(\omega_1 t)] E_1, \quad \mu_r = \frac{2}{E_1} \langle v(t) \cos(\omega_1 t) \rangle_t, \quad \mu_i = \frac{2}{E_1} \langle v(t) \sin(\omega_1 t) \rangle_t, \quad (6)$$

where  $\langle \dots \rangle_t$  denotes averaging over time. In practical terms, we need to average over a common period of the probe and pump ac fields. In the case of quasistatic fields the imaginary component  $\mu_i$  typically approaches zero [see, e. g., Eq. (20)], and thus we will focus on the behaviour of  $\mu \equiv \mu_r$  as a function of the pump field parameters. It is natural to scale  $\mu$  to the Drude mobility  $\mu_0 = 2v_p/E_{\text{cr}} = e\tau/m_0$  ( $m_0 = \frac{2\hbar^2}{\Delta d^2}$  is the effective electron mass at the bottom of the miniband). Note that the Drude mobility is related to the Drude conductivity  $\sigma_0$  as  $\mu_0 = \sigma_0/(eN)$ .

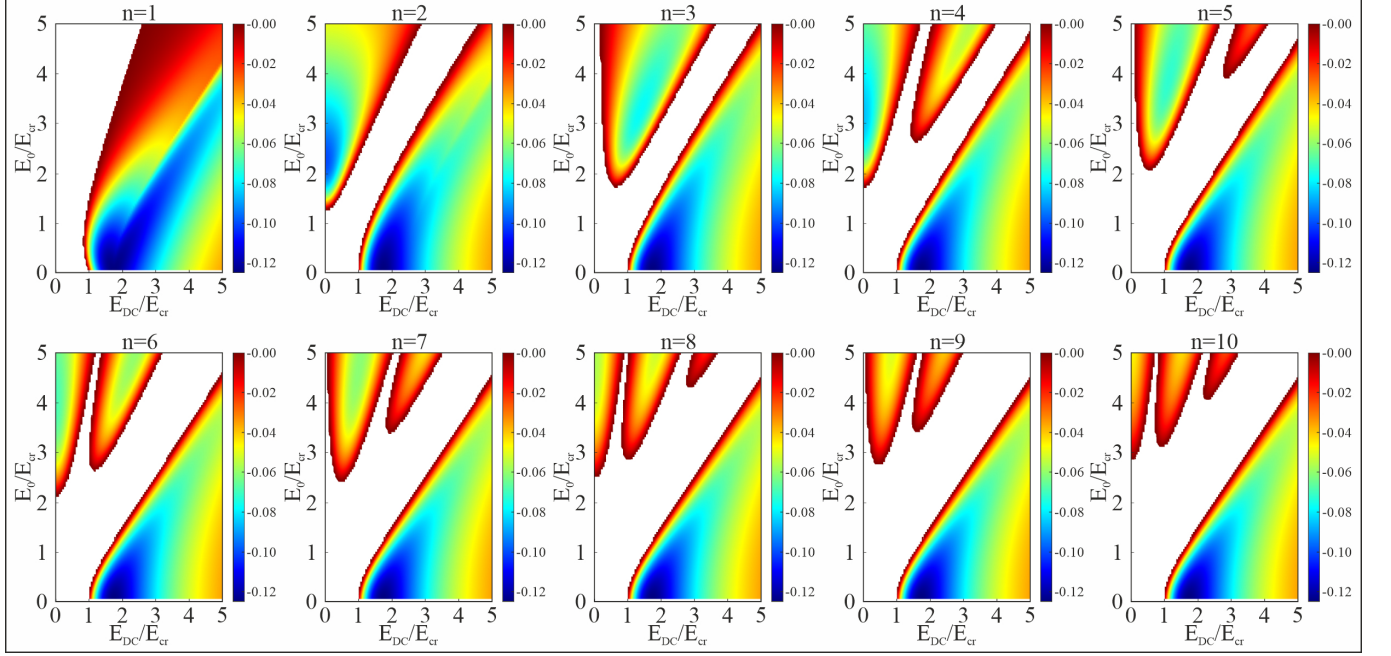


FIG. 4. Areas and magnitudes of the gain at optimal phase  $\mu_n^{\text{opt}}/\mu_0 < 0$  [Eq. (9)] in the plane of dc bias  $E_{\text{dc}}$  and pump field amplitude  $E_0$  for  $n = 1 : 10$ . The dc and ac electric fields are scaled to critical field  $E_{\text{cr}}$ . Blank areas correspond to absorption ( $\mu_n > 0$ ).

## B. Summary of the main results on HF mobilities

We found that for the both types of parametric amplification [Eqs. (3, 4)] the small-signal HF mobility  $\mu_n(\psi)$  can be represented as the following sum of the phase-independent *incoherent HF mobility*  $\mu_{\text{inc}}$  and the phase-dependent *coherent HF mobility*  $\mu_{\text{coh}}(\psi)$ :

$$\mu_n(\psi) = \mu_{\text{inc}} + \mu_{\text{coh}}(\psi), \quad \mu_{\text{inc}} = \mu_0 \left\langle \frac{(1 - F_p^2)}{(1 + F_p^2)^2} \right\rangle_T, \quad \mu_{\text{coh}}(\psi) = \mu_0 \left\langle \frac{(1 - F_p^2)}{(1 + F_p^2)^2} \cos(n\omega t) \right\rangle_T \cos \psi, \quad (7)$$

where  $F_p(t) = E_p(t)/E_{cr}$  is the scaled pump field [Eq. (2)], the sign  $\langle \dots \rangle_T$  denotes an average  $\frac{1}{T} \int_0^T dt$  over the period of the pump field  $T = 2\pi/\omega$ , and two other parameters (relative phase and parametric order) are

$$(\psi; n) = \left\{ \begin{array}{ll} (\phi_1 + \phi_2; n_+), & \text{see Eq. (3)} \quad (\text{nondegenerate sum}), \\ (\phi_1 - \phi_2; n_-), & \text{see Eq. (3)} \quad (\text{nondegenerate difference}), \\ (\phi; n_0), & \text{see Eq. (4)} \quad (\text{degenerate}). \end{array} \right. \quad (8)$$

The coherent gain reaches its maximum at an optimal phase  $\psi = \psi_{opt}$ , and the corresponding value of the total mobility  $\mu_n(\psi_{opt})$  is

$$\mu_n^{(opt)} = \frac{\mu_0}{2\pi} \int_0^{2\pi} \frac{(1 - F_p^2)}{(1 + F_p^2)^2} dx - \frac{\mu_0}{2\pi} \left| \int_0^{2\pi} \frac{(1 - F_p^2) \cos(nx)}{(1 + F_p^2)^2} dx \right|, \quad (9)$$

where  $F_p(x) = F_{DC} + F_0 \cos(x)$ . Note that the integrals in Eq. (9) can be taken analytically and result in cumbersome functions of complex variables [see Eq. (9) in [5]]. We underline that  $\mu_n^{(opt)}$  depends on the electric fields  $F_{DC} = E_{DC}/E_{cr}$  and  $F_0 = E_0/E_{cr}$ , but not on the pump frequency  $\omega_0$  itself. Figure 4 shows the areas of optimal gain  $\mu_n^{(opt)} < 0$  together with its magnitude in units of the Drude mobility  $\mu_0$  for different numbers of the pump photons  $n$ . This figure provides an extension of Fig. 3(a-b) of the main text for  $n > 2$ . Note that relative positions of the gain and absorption areas for  $n > 2$  are similar to those in the case  $n = 2$ .

In the coming subsections we will derive the Eqs. (7-9) for both the degenerate and nondegenerate schemes of amplification following the quasistatic approach of our earlier works [6, 7].

### C. Calculations of HF mobilities for the degenerate case

In the case of degenerate amplification, the HF mobility  $\mu_{n_0}(\phi)$  [cf. Eq. (6)] scaled to the Drude mobility  $\mu_0$  can be found as

$$\frac{\mu_{n_0}(\phi)}{\mu_0} = \frac{E_{cr} A(\phi)}{v_p E_1}, \quad A(\phi) = \langle v[E(t)] \cos(\omega_1 t + \phi) \rangle_t, \quad (10)$$

where  $E(t) = E_p(t) + E_{pr}(t)$  and the pump and probe electric fields are given by Eqs. (2,4), respectively. Following Eq. (10) we essentially need to calculate  $A(\phi)$ , and the amplification corresponds to  $A < 0$ . Since the probe electric field is weak, we can use the truncated Taylor series for the drift velocity

$$v(E) \approx v[E_p(t)] + v'[E_p(t)] E_1 \cos(\omega_1 t + \phi), \quad v'[E_p(t)] \equiv \left. \frac{\partial v}{\partial E} \right|_{E=E_p(t)} \quad (11)$$

and then substitute it in Eq. (10). This results in

$$A = A_h + A_{inc} + A_{coh} = \langle v[E_p(t)] \cos(\omega_1 t + \phi) \rangle_{2T} + (E_1/2) \langle v'[E_p(t)] \rangle_{2T} + (E_1/2) \langle v'[E_p(t)] \cos(2\omega_1 t + 2\phi) \rangle_{2T}. \quad (12)$$

For the electron velocity Eq. (5) and its derivative

$$\frac{\partial v}{\partial E} = \left( \frac{2v_p}{E_{cr}} \right) \frac{1 - (E/E_{cr})^2}{(1 + (E/E_{cr})^2)^2}, \quad (13)$$

the Eq. (12) can be further simplified to

$$A_{inc} = \langle v'[E_p(t)] \rangle_T \cdot (E_1/2), \quad A_{coh}(\phi) = \langle v'[E_p(t)] \cos(n_0 \omega t) \rangle_T \cos(2\phi) \cdot (E_1/2) \quad (14)$$

and  $A_h = \cos \phi \langle v[E_p(t)] \cos(\omega_1 t) \rangle_{2T} = 0$ . Now we substitute the derivative Eq. (13) in Eqs. (14) and then, following the findings of Eq. (10), divide the resulting equations by  $(v_p E_1/E_{cr})$ . In such a way we obtain the desirable form of HF mobility  $\mu_{n_0}(\phi)$  [see Eq. (7)].

The phase-dependant gain term  $A_{coh}(\phi) < 0$  has its maximal value ( $\max |A_{coh}|$ ) at some optimal phase  $\phi_{opt}$  that can be determined from the condition  $\frac{\partial A_{coh}}{\partial \phi} = 0$  as

$$\langle v'[E_p(t)] \cos(2\omega_1 t) \rangle_T \sin(2\phi_{opt}) = 0, \quad \phi_{opt} =: 0, \pi/2. \quad (15)$$

The exact value that  $\phi_{opt}$  takes for the given dc bias  $E_{DC}$  and the amplitude of ac pump  $E_0$  [Eq. (2)] depends on the sign of the integral involved in Eq. (15), as illustrated in Fig. 5 for the cases  $\omega_1/\omega = 3/2$  and  $5/2$ . Nevertheless, whatever is exact value of the optimal phase,  $A_{coh}(\phi_{opt})$  still has the form

$$A_{coh}(\phi_{opt}) = - \left| \langle v'[E_p(t)] \cos(n_0 \omega t) \rangle_T \right| \cdot (E_1/2). \quad (16)$$

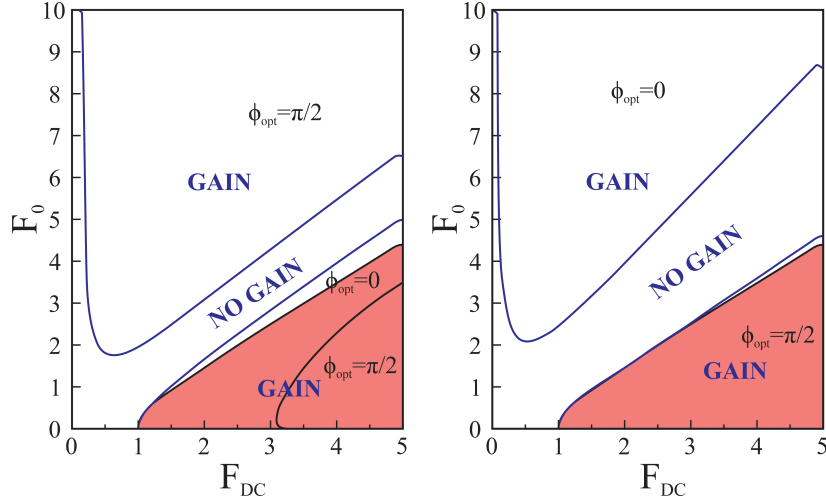


FIG. 5. Regions of the net small-signal gain  $A = A_{\text{inc}} + A_{\text{coh}} < 0$  [Eq. (12)] and the corresponding optimal phases  $\phi_{\text{opt}}$  [Eq. (15)] in the  $F_{\text{DC}} - F_0$  plane. Pink marks regions of the incoherent gain  $A_{\text{inc}} < 0$  [Eq. (14)]. Left panel:  $n_0 = 3$ , right panel:  $n_0 = 5$ .

#### D. Calculations of HF mobilities for the nondegenerate cases

To calculate gain in two nondegenerate cases  $\omega_1 \pm \omega_2 = n_{\pm}\omega$  [Eq. (3)] we essentially need to find (negative) values of the following integrals

$$A_{\omega 1} = \langle v[E(t)] \cos(\omega_1 t + \phi_1) \rangle_t, \quad A_{\omega 2} = \langle v[E(t)] \cos(\omega_2 t + \phi_2) \rangle_t, \quad (17)$$

where  $E(t) = E_p(t) + E_{\text{pr}}(t)$  and  $E_p(t)$ ,  $E_{\text{pr}}(t)$  are defined by Eqs. (2,3). Now  $E(t)$  is a quasiperiodic function of time, and therefore averaging in Eqs. (17) is performed over infinite time. Since the expressions of  $A_{\omega 1}$  and  $A_{\omega 2}$  are similar, we will only focus on the calculations related to  $A_{\omega 1}$ . For  $E_{1,2} \ll E_{0,\text{DC}}$  we make the expansion similar to Eq. (11) and obtain

$$\begin{aligned} A_{\omega 1} &= \langle v[E_p(t)] \cos(\omega_1 t + \phi_1) \rangle_t + \left\langle \frac{\partial v}{\partial E} \right|_{E_p(t)} \{E_1 \cos(\omega_1 t + \phi_1) + E_2 \cos(\omega_2 t + \phi_2)\} \cdot \cos(\omega_1 t + \phi_1) \Bigg\rangle_t = \\ &= \frac{E_1}{2} \left\langle \frac{\partial v}{\partial E} \right|_{E_p(t)} \Bigg\rangle_t + \frac{E_2}{2} \left\langle \frac{\partial v}{\partial E} \right|_{E_p} \cos(\omega_1 t + \omega_2 t) \Bigg\rangle_t \cos(\phi_1 + \phi_2) + \frac{E_2}{2} \left\langle \frac{\partial v}{\partial E} \right|_{E_p} \cos(\omega_1 t - \omega_2 t) \Bigg\rangle_t \cos(\phi_1 - \phi_2). \end{aligned} \quad (18)$$

By assuming that  $\omega_1 + \omega_2 = n_+\omega$  and  $\omega_1 - \omega_2 = n_-\omega$  are satisfied, we can represent Eq. (18) in the form

$$A^{(\omega 1)} = A_{\text{inc}}^{(\omega 1)} + A_{\text{coh}}^{(\omega 1)}(\phi_+) + A_{\text{coh}}^{(\omega 1)}(\phi_-),$$

$$A_{\text{inc}}^{(\omega 1)} = \langle v'[E_p(t)] \rangle_T \cdot (E_1/2), \quad A_{\text{coh}}^{(\omega 1)}(\phi_{\pm}) = \langle v'[E_p(t)] \cos(n_{\pm}\omega t) \rangle_T \cos(\phi_{\pm}) \cdot (E_2/2), \quad (19)$$

where  $\phi_{\pm} \equiv \phi_1 \pm \phi_2$  and the derivative  $v'(E)$  is given by Eq. (13). The optimal values of the phase  $\phi_+$  (or  $\phi_-$ ) are  $\phi_+^{\text{opt}} = 0, \pi$  [cf. Eq. (15)].

We see that the integrals involved in the incoherent terms  $A_{\text{inc}}$  for degenerate and nondegenerate cases are identical, while the corresponding coherent terms  $A_{\text{coh}}$  coincide when  $n_{\pm}$  are odd numbers [Eqs. (14) vs. Eqs. (19)]. Furthermore, for even values of  $n_{\pm}$  the mathematical structure of  $A_{\text{coh}}$  terms is still the same, and this allows us to represent all small-signal mobilities, derived within the quasistatic limit, as the universal expressions Eq. (7).

Finally, we want to demonstrate that the imaginary part of the HF mobility  $\sim \langle v[E(t)] \sin(\omega_1 t + \phi_1) \rangle_t$  [cf. Eq. (6)] vanishes. For this aim we again use the Taylor expansion for  $v(E)$ , substitute it in  $\langle v[E(t)] \sin(\omega_1 t + \phi_1) \rangle_t$ , and obtain

$$\langle v[E_p(t)] \sin(\omega_1 t + \phi_1) \rangle_t + \left\langle \frac{\partial v}{\partial E} \right|_{E_p(t)} \{E_1 \cos(\omega_1 t + \phi_1) + E_2 \cos(\omega_2 t + \phi_2)\} \cdot \sin(\omega_1 t + \phi_1) \Bigg\rangle_t =$$



$$= \frac{E_2}{2} \left\langle \frac{\partial v}{\partial E} \right|_{E_p} \cos(n_+ \omega t) \right\rangle_T \sin \phi_+ - \frac{E_2}{2} \left\langle \frac{\partial v}{\partial E} \right|_{E_p} \cos(n_- \omega t) \right\rangle_T \sin \phi_-, \quad (20)$$

which becomes zero when  $\phi_{\pm} \rightarrow \phi_{\pm}^{\text{opt}}$ .

#### IV. ESTIMATION OF THE PUMP ELECTRIC FIELD STRENGTH IN THE SL

Taking into account the impossibility to determine strength of the pump field inside the SL using current experimental setup, estimation, based on matching experimentally achieved emission power dependency on biasing voltage and above-described theoretical model, was performed in order to find at least approximate working point position.

Fitting the theoretical results given in Fig. 4 to experimental data one needs to note that several multiphoton processes undergo on the same time. Consequently, one can expect that the total mobility is a result of superposition of different multiphoton processes. Theoretical model, describing such superposition is an object of future investigations, but for the spectra, presented in Fig. 2 of the main body, these relations can be determined using emission power dependency on biasing voltage. Simple linear dependency was used as a point of departure:

$$\left( \frac{\mu}{\mu_0} \right)_{\text{total}} = \sum C_n \cdot \frac{\mu_n}{\mu_0} \quad (21)$$

where  $n$  is integer and  $C_n$  is weight coefficient. It is reasonable to assume that  $C_n$  will be inversely proportional to  $n$  indicating that mobilities with small  $n$  will give the essential influence for the final mobility dependence.

In order to get weight coefficients, emission power and mobility ratio dependence on biasing voltage profile equality was assumed. Arbitrary frequency of 21.20 GHz, corresponding to  $\frac{5}{2}\omega_0$  was selected and the emitted power dependency on biasing voltage along with its derivative were achieved [see Fig. 6(a)]. For simplicity relations were found including only  $n = 1, 2, 3$ . Influence of bigger  $n$  can be assumed as negligibly small. The final superposition relation was found to be as

$$\left( \frac{\mu}{\mu_0} \right)_{\text{total}} = 119 \cdot \frac{\mu_{n=1}}{\mu_0} + 18.9 \cdot \frac{\mu_{n=2}}{\mu_0} + 1 \cdot \frac{\mu_{n=3}}{\mu_0} \quad (22)$$

and results in mobility distribution, depicted in Fig. 6(b).

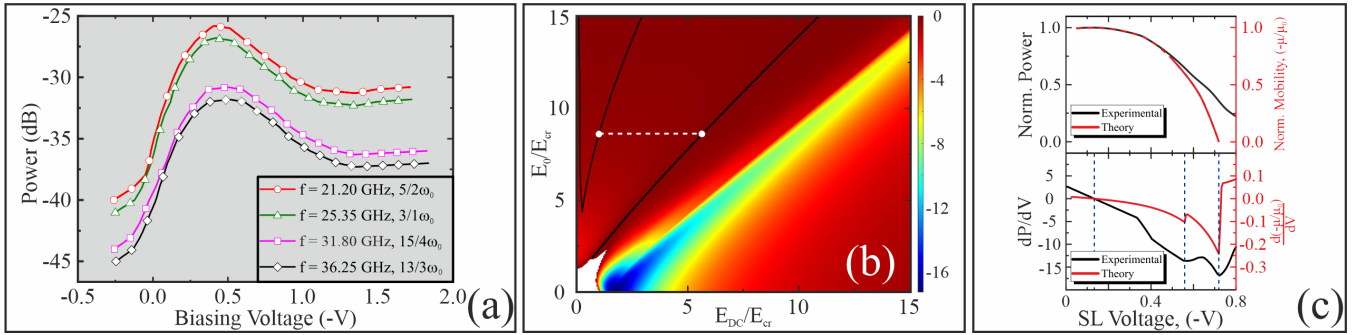


FIG. 6. (a): Emission power dependence on the SL bias voltage at different frequencies acquired using calibrated reference. Note equivalent evolution of all the spectral constituents the with DC bias. (b): Theoretical sketch of superpositioned mobility dependency on DC-biasing and microwave radiation field strength for  $5/2\omega_0$  frequency. Black lines represent mobility peak positions while white dotted line corresponds to the position of matched experimental profile. (c): superpositioned  $\mu_{\text{total}}(\phi_{\text{opt}})/\mu_0$  profile and its derivative for  $5/2\omega_0$  frequency for the estimated pump field strength ( $F_0 = 8.61$ ) in SL along with experimental results (built-in voltage included). Analysing derivative lines one can note that theoretical peak positions correspond for experimental data (see blue dashed lines).

One needs essentially to underline that experimental local derivative minima arise at the same voltage values as ones, obtained from theoretical model [see Fig. 6(c)]. Note that due to superposition no-gain region vanished comparing to the situation when the single  $n$  mobility distribution is analysed. Also, this calculation results in  $F_0 = 8.66$  alternating electric field strength across the superlattice.

## V. THE MEASURED INPUT-OUTPUT POWER DEPENDENCIES

The aim here is to present the emission power dependencies on the pump power (input-output plot) for subharmonics, arising due to multiphoton parametric processes in the SL, in comparison with the inherent process of frequency doubling.

The method of input-output characteristics is rather often used in nonlinear optics to analyse frequency multiplication and wave mixing phenomena. This indirect method is essentially based on comparison of experimental curves with the corresponding predictions of theoretical models. In the simplest case, the power at the frequency corresponding to  $n^{\text{th}}$  harmonic is featured by  $n^{\text{th}}$  power function dependence on the excitation power. Quadratic dependence was observed in experiments on optical second harmonic generation (see, e. g., [8] for in-cavity and [9] for cavityless SHG measurements). However, the input-output dependence typically becomes linear in the case of conventional optical parametric generation in a medium with a quadratic nonlinearity (cf. [10] for the theory and [11] for the experiment).

We emphasize that the superlattice in microwave electric field is not purely optical system – it is nonlinear optoelectronic system operating in the negative differential velocity regime with predominating multiphoton processes. The measured input-output dependencies for the studied superlattice are given in Fig. 7 for three characteristic processes: SHG, 5/2-harmonic generation and fractional (12/5) harmonic generation. In the small-signal limit (small output power), the later frequency results from a mixture of 6-photon down-conversion and 3-photon up-conversion processes [fig. 2 in the main body of the paper]. As one can see in Fig. 7, the input-output dependence of the second harmonic is seeking the square law, while the corresponding behaviour of both subharmonics is linear but with different slopes. In contrast to its optical counterpart [10], the existing theoretical model of dissipative parametric gain in the SL is still not in a mature state to predict the shape of the generated power at a given frequency as a function of the pump strength. Therefore, the input-output method is currently less informative in analysis of the dissipative gain than the direct spectroscopic approach.

In summary, the measured difference in dependencies between the input and output powers together with the spectroscopic analysis provide convincing experimental evidence of the multiphoton parametric processes.

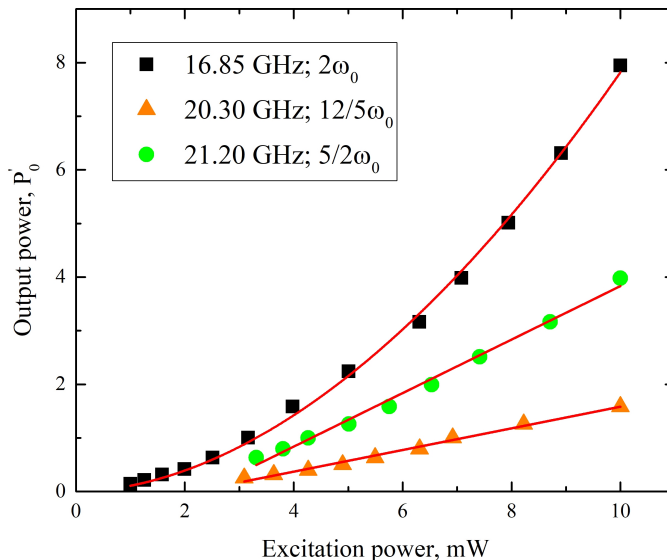


FIG. 7. Input-output plots for the superlattice device demonstrating dissipative parametric gain. There is no external voltage bias; the pump frequency is 8.45 GHz. Notice that the corresponding dependencies for degenerate and nondegenerate multiphoton parametric processes can be approximated by the straight lines with different gradients.

## VI. FIGURE 2 DATA IN THE FORM OF TWO TABLES

The tables below represent data used in Fig. 2 of the main text. All frequencies are in GHz; the frequency ratios (fractions) are defined with respect to the pump frequency  $\omega_0/2\pi = 8.45$  GHz.

TABLE I. Expanded relations of multiphoton and multiple wave mixing phenomena, related to Fig. 2 main panel.

Frequency	Fraction		Frequency	Fraction		$n_{\pm}$	Excitation frequency
11.20	(4/3)	+	23.05	(8/3)	=	4	$\times$ 8.45
12.67	(3/2)	+	21.20	(5/2)	=	4	$\times$ 8.45
14.46	(7/4)	+	18.98	(9/4)	=	4	$\times$ 8.45
13.45	(8/5)	+	20.30	(12/5)	=	4	$\times$ 8.45
18.98	(9/4)	+	23.05	(11/4)	=	5	$\times$ 8.45
13.45	(8/5)	+	28.20	(17/5)	=	5	$\times$ 8.45
23.05	(8/3)	+	28.20	(10/3)	=	6	$\times$ 8.45
14.46	(7/4)	+	36.25	(17/4)	=	6	$\times$ 8.45
18.98	(9/4)	+	31.80	(15/4)	=	6	$\times$ 8.45
18.98	(11/5)	+	31.80	(19/5)	=	6	$\times$ 8.45
23.05	(8/3)	+	36.25	(13/3)	=	7	$\times$ 8.45
23.05	(11/4)	+	36.25	(17/4)	=	7	$\times$ 8.45
31.80	(15/4)	+	36.25	(17/4)	=	8	$\times$ 8.45
31.80	(19/5)	+	36.25	(21/5)	=	8	$\times$ 8.45

36.25	(13/3)	-	28.20	(10/3)	=	1	$\times$ 8.45
21.20	(5/2)	-	12.67	(3/2)	=	1	$\times$ 8.45
31.80	(15/4)	-	23.05	(11/4)	=	1	$\times$ 8.45
23.05	(11/4)	-	14.46	(7/4)	=	1	$\times$ 8.45
28.20	(17/5)	-	20.30	(12/5)	=	1	$\times$ 8.45
28.20	(10/3)	-	11.20	(4/3)	=	2	$\times$ 8.45
36.25	(17/4)	-	18.98	(9/4)	=	2	$\times$ 8.45
36.25	(21/5)	-	18.98	(11/5)	=	2	$\times$ 8.45
31.80	(15/4)	-	14.46	(7/4)	=	2	$\times$ 8.45
36.25	(13/3)	-	11.20	(4/3)	=	3	$\times$ 8.45

TABLE II. Expanded classification of the generated frequencies according to the pump fractions (see inset of Fig. 2).

Line number	Frequency	2.5% accuracy fractions		
1	8.45	1/1 (0.00%)		
2	11.20	4/3 (0.59%)		
3	12.67	3/2 (0.04%)		
4	13.45	8/5 (0.52%)		
5	14.46	7/4 (2.21%)		
6	16.85	2/1 (0.30%)		
7	18.98	9/4 (0.17%)	11/5 (2.08%)	
8	20.30	12/5 (0.10%)		
9	21.20	5/2 (0.35%)		
10	23.05	11/4 (0.81%)	8/3 (2.27%)	
11	25.35	3/1 (0.00%)		
12	28.20	10/3 (0.12%)	17/5 (1.86%)	
13	31.80	15/4 (0.35%)	19/5 (0.97%)	
14	33.98	4/1 (0.53%)		
15	36.25	17/4 (0.94%)	13/3 (1.01%)	21/5 (2.12%)

- 
- [1] L. Subačius, K. Jarašiūnas, P. Ščajev, and M. Kato, Development of a microwave photoconductance measurement technique for the study of carrier dynamics in highly-excited 4h-sic, *Measurement Science and Technology* **26**, 125014 (2015).
- [2] A. A. Ignatov, V. I. Piskarev, and V. I. Shashkin, Instability (formation of domains) of an electric-field in multilayer quantum structures, *Sov. Phys. Semicond.* **19**, 1345 (1985).
- [3] P. G. Savvidis, B. Kolasa, G. Lee, and S. J. Allen, Resonant crossover of terahertz loss to the gain of a bloch oscillating InAs/AlSb superlattice, *Phys. Rev. Lett.* **92**, 196802 (2004).
- [4] B. Rieder, *Semiclassical transport in semiconductor superlattices with boundaries*, Ph.d. thesis, University of Regensburg (2004).
- [5] Y. Y. Romanova, Parametric generation of high-frequency harmonics in semiconductor superlattices, *Semiconductors* **96**, 1451 (2012).
- [6] A. V. Shorokhov and K. N. Alekseev, High-frequency absorption and gain in superlattices: Semiquasistatic approach, *Physica E: Low-dimensional Systems and Nanostructures* **33**, 284 (2006).
- [7] K. N. Alekseev, M. V. Gorkunov, N. V. Demarina, T. Hyart, N. V. Alexeeva, and A. V. Shorokhov, Suppressed absolute negative conductance and generation of high-frequency radiation in semiconductor superlattices, *EPL* **73**, 934 (2006).
- [8] C. Wang, M. J. Burek, Z. Lin, H. A. Atikian, V. Venkataraman, I. Huang, P. Stark, and M. Lončar, Integrated high quality factor lithium niobate microdisk resonators *Optics Express* **22**, 30924-30933 (2014).
- [9] H. Zhao, Q. An, X. Ye, B. H. Yu, Q. H. Zhang, F. Sun, Q. Y. Zhang, F. Yang, J. Guo, and J. Zhao., Second harmonic generation in AB-type LaTiO<sub>3</sub>/SrTiO<sub>3</sub> superlattices, *Nano Energy* **82**, 105752 (2021).
- [10] R. Byer, Quasi-Phasematched Nonlinear Interactions and Devices, *Journal of Nonlinear Optical Physics and Materials* **6**, 549-592 (1997).
- [11] Y. Du, S. N. Zhu, Y. Y. Zhu, P. Xu, C. Zhang, Y. B. Chen, Z. W. Liu, N. B. Minget, X. R. Zhang, F. F. Zhang, and S. Y. Zhang, Parametric and cascaded parametric interactions in a quasiperiodic optical superlattice, *Appl. Phys. Lett.* **81**, 1573-1575 (2002).